RESEARCH ARTICLE

Magnetic Resonance in Medicine

Thermal noise lowers the accuracy of rotationally invariant harmonics of diffusion MRI data and their robustness to experimental variations

Guillem París¹ | Tomasz Pieciak¹ | Derek K. Jones² | Santiago Aja-Fernández¹ | Antonio Tristán-Vega¹ | Jelle Veraart³

¹Laboratorio de Procesado de Imagen, ETSI Telecomunicación, Universidad de Valladolid, Valladolid, Spain

²Cardiff University Brain Research Imaging Centre, Cardiff University, Cardiff, UK

³Center for Biomedical Imaging, NYU Grossman School of Medicine, New York City, New York, USA

Correspondence

Guillem París, Laboratorio de Procesado de Imagen, ETSI Telecomunicación, Universidad de Valladolid, Valladolid, Spain.

Email: guillem.paris@uva.es

Funding information

National Institute of Neurological Disorders and Stroke, Grant/Award Number: R01 NS088040; Narodowa Agencja Wymiany Akademickiej, Grant/Award Number: PPN/BEK/2019/1/00421; Consejería de Educación, Junta de Castilla y León, Grant/Award Number: Orden EDU/1100/2017 12/12; EPSRC Centre for Doctoral Training in Medical Imaging, Grant/Award Number: EP/M029778/1; Agencia Estatal de Investigación, Grant/Award Numbers: PID2021-124407NB-I00, TED2021-130758B-I00; Junta de Castilla y León, Grant/Award Number: VA156P24; European Social Fund Plus; Krajowy Naukowy Osrodek Wiodacy, Grant/Award Number: 692/STYP/13/2018; National Institute of Biomedical Imaging and Bioengineering, Grant/Award Number: NIH P41 EB017183

Abstract

Purpose: Rotational invariants (RIs) are at the root of many dMRI applications. Among others, they are presented as a sensible way of reducing the dimensionality of biophysical models. While thermal noise impact on diffusion metrics has been well studied, little is known on its effect on spherical harmonics-based RI (RISH) features and derived markers. In this work, we evaluate the effect of noise on RISH features and downstream Standard Model Imaging (SMI) estimates.

Theory and Methods: Using simulated and test/retest multishell MRI data, we assess the accuracy and precision of RISH features and SMI parameters in the presence of thermal noise, as well as its robustness to variations in protocol design. We further propose and evaluate correction strategies that bypass the need of rotational invariant features as an intermediate step.

Results: Both RISH features and SMI estimates are impacted by SNR-dependent Rician biases. However, higher-order RISH features are susceptible to a secondary noise-related source of bias, which not only depends on SNR, but also protocol and underlying microstructure. Rician bias-correcting techniques are insufficient to maximize the accuracy of RISH and SMI features, or to ensure consistency across protocols. SMI estimators that avoid RISH features by fitting the model to the directional diffusion MRI data outperform RISH-based approaches in accuracy, repeatability, and reproducibility across acquisition protocols.

Conclusions: RISH features are increasingly used in dMRI analysis, yet they are prone to various sources of noise that lower their accuracy and reproducibility. Understanding the impact of noise and mitigating such biases is critical to maximize the validity, repeatability, and reproducibility of dMRI studies.

KEYWORDS

 $biophysical\ models,\ diffusion\ weighted\ imaging,\ Rician\ bias,\ rotational\ invariants,\ standard\ model\ imaging$

This is an open access article under the terms of the Creative Commons Attribution-NonCommercial License, which permits use, distribution and reproduction in any medium, provided the original work is properly cited and is not used for commercial purposes.

© 2025 The Author(s). Magnetic Resonance in Medicine published by Wiley Periodicals LLC on behalf of International Society for Magnetic Resonance in Medicine.

1 | INTRODUCTION

Diffusion MRI (dMRI) has been demonstrated to be a powerful method to non-invasively probe brain microstructure at a sub-voxel resolution. Its metrics are sensitive to microstructural changes in the brain related to development, maturation, aging, and pathology. However, the clinical utility of dMRI remains challenged by a lack of specificity of the diffusion-weighted contrast to microstructural features such as demyelination, axonal loss, or inflammation.

Such lack of specificity is being addressed through the development of biophysical models by decomposing the macroscopic diffusion-weighted (DW) signal in a set of compartments with presumed morphological and diffusion characteristics. ¹² Typically, said models propose to estimate microstructural information of multiple parameterized compartments by fitting a given diffusion model onto DW data acquired with various b-values, gradient directions, ^{12–17} and possibly diffusion times, ^{18,19} echo times, ²⁰ or tensor encodings. ²¹

Biophysical models of diffusion in anisotropic brain white-matter tissue have a high dimensionality given the necessity to parametrize the fiber orientation distribution function (fODF), possibly resulting in poor precision and robustness.^{22,23} An initial strategy to reduce the number of model parameters of biophysical models is the adoption of simplified models of the fODFs, such as Watson or Bingham distribution, with the risk of reduced validity. 16,24,25 Alternatively, the dimensionality of biophysical models can be reduced by extracting rotationally invariant signal features that encode the microstructural information of fiber fascicles, but not the macroscopic orientation distribution function of such fascicles, disentangling microstructural properties from their orientation distribution function (ODF). 12,26,27 In other words, rotationally invariant features, typically derived from the spherical harmonic (SH) representation of the DW signal, are agnostic to any kind of rotation that data might endure, thus removing the directional dependency of the signal.

Today, rotationally invariant signal features form the basis of numerous biophysical models of the white matter^{27–30} or the gray matter.^{18,19} Common examples include the spherical mean technique,³¹ standard model imaging (SMI),²³ axon diameter mapping,³² free water imaging,^{33,34} SANDI,¹⁸ neurite exchange imaging model (NEXI),¹⁹ and standard model with exchange (SMEX).³⁵ Within the context of modeling, the most commonly used rotationally invariant signal feature is the "spherical mean,"^{26,31} which corresponds to the zeroth-order SH coefficient, but the use of higher orders has recently been promoted, as it provides complimentary information.^{23,27,29,36,37} Therefore, for anisotropic tissue,

including higher-order rotational invariants, such as l=2 or above, provides additional information to resolve the model while lowering the necessity for numerous b-shells, thereby making biophysical models compatible with many publicly available data sets.³⁸

Alongside their use in biophysical modeling, rotationally invariant features are also used as sensitive biomarkers in the analysis of diffusion MRI data^{7,39,40} as features to drive data harmonization across scanners and protocols^{26,41,42} and to train deep learning tools.³⁹ As we witness an increased use of rotationally invariant signal features for a variety of analysis approaches, it becomes increasingly important to understand the confounds in its quantification, including its robustness to experimental factors such signal-to-noise ratio (SNR) or protocol design.

Despite increasing attempts to achieve higher SNR through hardware and software improvements, such as increasing field strengths, 43 stronger imaging gradients, 44 better receiver coil arrays, 45 and denoising, 46 dMRI is an imaging technique that is intrinsically poor in SNR. Thermal noise affects the quantification of diffusion metrics in various ways, with eigenvalue repulsion⁴⁷ and Rician signal biases⁴⁸ being notorious examples. Under some often-met conditions, diffusion MRI data are Rician-distributed. Therefore, the expectation value of the signal is higher than the noise-free underlying signal. This bias, often referred to as Rician signal bias, is stronger at lower SNR and results in an SNR-dependent misestimation of apparent diffusivities, fractional anisotropy (FA), and kurtosis values if parameter estimators do not explicitly account for the actual probability distribution function of magnitude MRI data. 48,49 In the context of biophysical modeling, Rician signal biases have been associated with a still water fraction.⁵⁰ Yet, little is known on the effect of noise on rotational invariants and its downstream effect on derived biophysical model parameters.

In this work, we assess the effect of thermal noise on rotational invariants via both simulated and in vivo data. We also evaluate the effect of noise in downstream biophysical models that are derived from such rotational invariants by considering the SMI microstructural parameters. Finally, we propose and evaluate correction strategies.

2 | THEORY

2.1 Rotationally invariant spherical harmonic features

The attenuation signal $S(b, \mathbf{g})$, acquired for a diffusion-weighting strength b and gradient direction \mathbf{g} , can be represented as

5222594, 0, Downloaded from https://onlinelibrary.wiley.com/doi/10.1002/mrm.70035 by Universidad De Valladolid, Wiley Online Library on [06/10/2025]. See the Terms and Conditions (https:/

$$S(b, \mathbf{g}) = \frac{1}{S(0)} \int_{|\mathbf{n}|=1} d\mathbf{n} \, \mathcal{P}(\mathbf{n}) \mathcal{K}(b, \mathbf{g}^T \mathbf{n}), \tag{1}$$

where $\mathcal{P}(\boldsymbol{n})$ is the fODF, normalized so that $\int d\boldsymbol{n} \mathcal{P}(\boldsymbol{n}) \equiv 1$, and \mathcal{K} is the signal response kernel of a fascicle aligned to the direction \boldsymbol{n} . Similar to Novikov et al., we normalize $d\boldsymbol{n} = \frac{\sin(\theta)d\theta d\varphi}{4\pi}$ so that $\int d\boldsymbol{n} = 1$. The fODF $\mathcal{P}(\boldsymbol{n})$ is typically parameterized by means of its projection onto the SH, such that

$$\mathcal{P}(\boldsymbol{n}) = 1 + \sum_{l=2}^{\infty} \sum_{(l \text{ even})}^{l} \sum_{m=-l}^{l} p_{lm} Y_{lm}(\boldsymbol{n}), \tag{2}$$

where p_{lm} are the coefficients in the SH basis, as follows:

$$Y_{lm}(\mathbf{n}) = \sqrt{\frac{2l+1}{4\pi} \frac{(l-m)!}{(l+m)!}} P_{lm}(\cos(\theta)) e^{im\varphi}, \qquad (3)$$

where $n = [\theta, \varphi]$, $\theta \in [0, \pi]$ and $\varphi \in [0, 2\pi)$, and $P_{lm}(x)$ is the generalized Legendre polynomial with degree l and order m. Notice that only real SH (even orders of l) are being introduced under the assumption of antipodally symmetric diffusion.⁵¹

Similarly, for a given *b*-value, $S(b, \mathbf{g})$ samples the signal orientation distribution function, which can also be parameterized in such SH basis using SH coefficients $S_{lm}(b)$, as follows:

$$S(b, \mathbf{g}) = \sum_{l=0}^{\infty} \sum_{(l \text{ even})}^{l} \sum_{m=-l}^{l} S_{lm}(b) Y_{lm}(\mathbf{g}). \tag{4}$$

Although $S_{lm}(b)$ are dependent on the orientation of the underlying microstructure, we can derive SH-rotational invariants (RISH) of the *l*th order S_l as follows:

$$S_l(b) = \frac{1}{N_l} \sqrt{\sum_{m=-l}^{l} |S_{lm}(b)|^2},$$
 (5)

where $N_l = \sqrt{4\pi(2l+1)}$ is a normalization parameter. ^{23,26,27} We limit ourselves to the zeroth and second-order RISH features (l=0 and l=2), given that the signal contribution of higher-order terms decays exponentially fast, therefore resulting in

$$S_0(b) = \sqrt{\frac{1}{4\pi}} S_{00}(b), \tag{6}$$

and

$$S_2(b) = \sqrt{\frac{1}{20\pi} \sum_{m=-2}^{2} \left[S_{2m}(b) \right]^2}.$$
 (7)

Note that S_0 is often referred to as the spherical mean. The value of S_2 , on the other hand, is closely related to the recently introduced spherical variance.²⁹

2.2 | Biophysical modeling

2.2.1 | Model

The SMI draws an overarching picture of biophysical models that describe DW signal as a sum of nonexchanging Gaussian compartments.²³ The signal kernel \mathcal{K} of Eq. (1) is defined as follows:

$$\mathcal{K}(b,\zeta) = S(0) \left[f \exp\left(-bD_a\zeta^2\right) \right]$$

$$+ S(0) \left[(1-f) \exp\left(-bD_e^{\perp} - b\left(D_e^{\parallel} - D_e^{\perp}\right)\zeta^2\right) \right],$$
(8)

where S(0) = S(b=0) is the average baseline signal, and $\zeta = \mathbf{g}^T \mathbf{n}$ depicts the relative angle between the gradient direction and the fascicle (i.e., $\cos\theta = \mathbf{g}^T \mathbf{n}$). The kernel parameters, corresponding to the microstructural parameters to be estimated within the white matter, are defined as the intracellular signal fraction f, longitudinal intra-cellular diffusivity D_a , extracellular parallel D_e^{\parallel} , and perpendicular D_e^{\perp} diffusivities. Note that intracellular perpendicular diffusivity is assumed to be zero.⁵²

Following the parameterization of the fODF in the SH basis, Eq. (1) can be rewritten as

$$S(b, \mathbf{g}) = \sum_{l=0}^{\infty} \sum_{(l \text{ even})}^{l} \sum_{m=-l}^{l} p_{lm} K_l(b; \boldsymbol{\theta}) Y_{lm}(\mathbf{g}), \tag{9}$$

where K_l is the projection of the response kernel onto the Legendre polynomials for a given set of parameters $\theta = \{f, D_a, D_e^{\parallel}, D_e^{\perp}\}$, as per Funk-Hecke's theorem.⁵³

We can further simplify this equation by representing $S(b, \mathbf{g})$ in the SH basis, as follows:

$$S_{lm}(b) = p_{lm}K_l(b;\theta), \tag{10}$$

or the derived rotational-invariant features as follows:

$$S_l(b) = p_l K_l(b; \theta), \tag{11}$$

where
$$p_{l} = \frac{1}{N_{l}} \sqrt{\sum_{m=-l}^{l} |p_{lm}|^{2}}$$
.

The fODF rotational invariants p_l are either defined as $p_0 = 1$ or estimated as part of the microstructural parameters that measure the coherence of the fODF p_2 .

Note that, for l=0, the number of parameters is 4 $(f, D_a, D_e^{\parallel}, D_e^{\perp})$, whereas for $l \geq 2$, additional modeling

parameters p_l have to be estimated. The coherence index p_2 varies between 0 and 1. For a fully isotropic fODF, $p_2 = 0$, although a delta function on a sphere, has $p_2 = 1$.

2.2.2 | Fitting

Given the multitude of SMI representations, such as Eqs. (9) and (11), it is clear there is no unique way of model fitting to extract the parameters of interest from dMRI data.

The biophysical model parameter vector θ is most estimated by minimizing the equation as follows:

$$\widehat{\boldsymbol{\theta}}^{(2)} = \arg\min_{\theta} \sum_{j=1}^{N_b} \sum_{l=0}^{L} \frac{1}{(l \text{ even})} \frac{1}{\sigma_{lj}^2} |S_l(b_j) - p_l K_l(b_j; \boldsymbol{\theta})|^2, \quad (12)$$

where b_j is the b-value for each of the N_b DW shells; L is the maximum SH degree; and $\sigma_{lj}^2 \sim (2l+1)/N_g$ weights to compensate for the heteroscedasticity, with N_g being the number of diffusion gradients in the jth shell. ²³ In its essence, this presents a two-step fitting process SH-SMI, referencing the intermediate step of estimated SH coefficients $S_{lm}(b)$ and derived rotation-invariants $S_0(b)$ and $S_2(b)$. The value of $S_{lm}(b)$ is commonly estimated using linear least squares (LLS) estimators, as it is computationally efficient and various software libraries provide open-source implementations of such estimators (e.g., MRtrix), ⁵⁴ as follows:

$$\widehat{S}_{lm}(b) = \arg\min_{c} \sum_{j=1}^{N_g} \left(S(b, g_j) - c Y_{lm}(\mathbf{g}_j) \right)^2, \tag{13}$$

which has a trivial closed-form solution. Note that N_g is the number of DW signals with b-value b. This two-step fitting process is commonly used in many of the listed models (e.g., SMT,³¹ SMI,²³ SANDI,¹⁸ NEXI,¹⁹ SMEX³⁵).

Alternatively, one can bypass the intermediate step of computing rotational invariants. Following Eq. (9), we can estimate the model parameters, alongside the fODF, directly from the DW data $S(b, \mathbf{g})$ using the following nonlinear least-squares estimator:

$$\widehat{\boldsymbol{\theta}}^{(1)} = \arg\min_{\boldsymbol{\theta}} \sum_{j=1}^{N} \left(S(b_j, \mathbf{g}_j) - \sum_{l=0}^{L} \sum_{(l \text{ even})}^{l} \sum_{m=-l}^{l} p_{lm} K_l(b; \boldsymbol{\theta}) \right)^2.$$
(14)

This single-step fitting (or direct fit, DF) strategy was initially proposed by Jespersen et al.¹⁵ Although SH-based modeling approaches gained interest, preliminary results suggested the effect of direct fitting in settings where DW data are not acquired in conventional *b*-shells, by design or due to gradient nonlinearities.⁵⁵

The estimators of $\hat{S}_{lm}(b)$ and $\hat{\boldsymbol{\theta}}^{(1)}$ are (asymptotically) unbiased if the DW data $S(b, \boldsymbol{g})$ are Gaussian-distributed.

2.3 | Data distributions

2.3.1 | Rician distribution of dMRI data

The reconstruction of DW images typically includes the computation of the magnitude of the otherwise normally distributed, complex-valued MR image. Their phase—sensitive to macroscopic tissue motion due to cardiac pulsation, perfusion, and others—varies from image to image, and impedes further modeling if not corrected or omitted. For In computing the magnitude s, its distribution is no longer Gaussian, but Rician under some often-met conditions. Therefore, the probability density function $p(s|v,\sigma)$ of magnitude MRI data is then

$$p(s, \nu | \sigma) = \frac{s}{\sigma^2} \exp\left(-\frac{s^2 + \nu^2}{2\sigma^2}\right) I_0\left(\frac{s\nu}{\sigma^2}\right), \quad s \ge 0, \quad (15)$$

where ν is the noiseless signal amplitude; σ the Gaussian noise standard deviation; and I_0 is the zeroth-order modified Bessel function of the first kind. ^{57,58} Its conditional expectation is given by the following formula:

$$E[s|\nu,\sigma] = \mu = \sigma \cdot \sqrt{\frac{\pi}{2}} \cdot L_{1/2} \left(\frac{-\nu^2}{2\sigma^2}\right)$$
 (16)

where $L_{1/2}$ is Laguerre's polynomial. The positive offset between μ and ν is SNR-dependent, exacerbated on the low-intensity data points such as those acquired in higher b-values, and often referred to as the Rician signal bias. This signal bias affects the accuracy of the estimated model parameters. $^{47-49,59,60}$

2.3.2 | Correction approaches

Common estimators, such as least squares estimators, are biased if the data are Rician-distributed. The magnitude of the bias is SNR-dependent but cannot be ignored if any of the DW signals has an SNR below 2.⁵⁸ To address this issue, various strategies have been presented to mitigate the bias either (i) by lowering the initial noise level in the complex^{61,62} or spatial domain^{37,63} or (ii) by mitigating its propagation to the dMRI metrics by means of maximum likelihood estimators,^{57,64} conditional least squares (CLS),⁶⁵ or signal transformations.⁶⁶

In this work, we make use of a CLS implementation embedding the Rician expectation (Eq. [16]) to offset model predictions^{50,65}:

$$v_{CLS} = \arg\min_{v} \sum_{i}^{N} (s_i - E[s, v | \sigma])^2$$
 (17)

where s_i are the observed signals, and the model prediction term is replaced by their corresponding Rician expectation with v being the model prediction itself and σ the Gaussian noise standard deviation. We will here refer to Rician bias correction (RBC) when using this approach.

Such estimator is a generic approach that can be adopted to estimate $\hat{S}_{lm}(b)$ or $\hat{\theta}^{(1)}$ by modifying Eqs. (13) and (14) accordingly. Unlike maximum likelihood estimators, we model the signal offset due to the Rician signal bias using its expectation value only, thereby ignoring higher-order terms of the data distribution. As demonstrated by Veraart et al., such an approach is suitable even when image preprocessing methods alter the data distribution, as long as the expectation value is preserved.⁶⁵ Common examples include data interpolation in a locally homogeneous neighborhood⁶⁵ or image denoising using MPPCA.67

2.3.3 Noncentral Chi distribution of RISH features

Note that the $\hat{S}_{lm}(b)$ coefficients are not noise-free. Indeed, they are asymptotically normal (under the central limit theorem) with their standard deviation dependent on σ and scan protocol, such as number of gradient directions. The rotational invariant S_0 will thus be (asymptotically) Gaussian distributed. However, assuming the same variance on each of these S_{2m} coefficients (with m ranging from -2 to 2), the S_2 follows a noncentral Chi distribution.⁵⁷ Similar to the Rician distribution, the expectation value of the noncentral Chi distribution exceeds its underlying noise-free value. Therefore, $\hat{S}_2(b)$ is prone to a systematic numeric bias that depends on the noise level of $\hat{S}_{lm}(b)$, which is affected by various factors, including SNR of data, data preprocessing steps such as denoising, and scan protocol. Note that this source of bias is complementary to any errors that arise from Rician signal biases.

3 **METHODS**

3.1 In silico data

We evaluated the properties of the various estimates using simulated data for varying b-values, gradient directions, biophysical model parameters, fiber configurations, and SNR values. Equation (9) was used as a forward model to generate simulated DW signals for given parameters, setting $L_{max} = 6$. For crossing fiber configurations, we

generated DWI signals for two fascicles that are rotated with respect to each other by a rotation angle α , but identical otherwise. These signals were added with relative weight w before adding noise. We added complex Gaussian noise with $\sigma = 1/SNR$, for different SNR values, before computing the signal's magnitude. 65 The resulting DW data are Rician-distributed.⁵⁸ All parameter settings are specified when relevant in the following sections. However, briefly, SNR varied between 5 and 45 in our experiments. In agreement with our in vivo MRI data, b-values were generally set to [0.5, 1, 2.5, 6] ms/µm². Unless specified otherwise, the biophysical model parameters were uniformly sampled within the following ranges: $f \in [0.25, 0.75], D_a \in [0.5, 2.5] \mu \text{m}^2/\text{ms}$, $D_{e}^{\parallel} \in [0.5, 2.5] \ \mu \text{m}^{2}/\text{ms}, \ D_{e}^{\perp} \in [0.1, 1] \ \mu \text{m}^{2}/\text{ms}, \ \text{and} \ p_{2} \in$ [0,1]. Moreover, the elevation angle between two simulated fibers was randomly set to $\alpha \in \left[0, \frac{\pi}{2}\right]$. Finally, the number of gradient directions was set to 32.

3.2 In vivo data set

3.2.1 Data acquisition

This study presents the secondary analysis of test/retest dMRI data^{32,68} of 5 healthy adult volunteers who were previously collected under the approval of the Cardiff University School of Psychology Ethics Committee. All data were acquired on a Siemens Connectom 3T MRI scanner using a 32-channel receiver coil. Subjects underwent a test and retest scans during the same visit, but they were repositioned between the scans. All dMRI data were acquired with a multiband blipped-CAIPI accelerated (simultaneous multislice = 2) echo-planar imaging sequence. The acquisition was further accelerated using GRAPPA acceleration (R=2), using adaptive combine reconstruction to obtain Rician-distributed results.⁶⁹ All images were acquired with repetition time/echo time = 3500/66 ms and an in-plane spatial resolution of $2.5 \times 2.5 \,\mathrm{mm}^2$ and slice thickness of 2.5 mm. In addition to 23 non-DWI, DW images were recorded by applying diffusion gradients with $\Delta/\delta = 30/15$ ms and varying gradient amplitude. The acquisition distributed DWIs across the following b-shells: 0.5, 1.0, 2.5, and $6.0 \,\mathrm{ms/\mu m^2}$. The corresponding number of gradient directions, distributed on a sphere, were 30, 30, 30, and 120, respectively. The last shell, however, was acquired in two sets of 60 uniformly distributed gradients. Ten non-DW images with reversed phase encoding were acquired in support of susceptibility-induced geometrical distortion correction.

3.2.2 | Data preprocessing

Preprocessing of the data included detection and removal of signal outliers 70 and the corrections for Gibbs ringings, 71 subject motion, and susceptibility and eddy current distortions. 72 Gradient nonlinearities were corrected by scaling the *b*-values voxel-by-voxel. 73 The noise level was estimated from the data acquired with b-values up to $1 \text{ ms/} \mu \text{m}^2$ using MPPCA with a window size of [5, 5, 5] to avoid Rician biases in the noise map. 67

3.2.3 | Region-of-interest analysis

We performed image registration using the ANTsRegistrationSyN tool (ANTs toolbox) between the subject's FA map and the JHU FA template (JHU-ICBM-FA-1 mm). The registration was only computed for the subject's test data and includes both an affine transformation and a diffeomorphic warp field. The JHU labels (JHU-ICBM-labels-1 mm; Analysis Group, FMRIB, Oxford, UK)⁷⁴ were then transformed into the subject's space by applying the inverse transformation using nearest-neighbor interpolation. We accounted for any misalignment between the test and retest data using an additional rigid registration transformation. Each of the white-matter regions of interest (ROIs) was then masked by means of threshold masks of the white-matter tract density imaging, 75 removing voxels that were not intersected by tracts, and thus possibly representing gray matter or cerebrospinal fluid. Finally, ROIs containing less than 50 voxels were discarded. A representative of each region (a total of 27 of the 48 original labels) was computed as the median for each SMI estimate. An overview of the included ROIs is listed in Table S1.

3.3 | Parameter estimation

The microstructural parameters within the SMI framework are estimated by means of two estimation strategies, which are derived from Eqs. (6), (7), (12), and (14), respectively. In the first approach, $\hat{\theta}^{(2)}$, we first estimate $\hat{S}_{lm}(b)$ and derive the corresponding $\hat{S}_0(b)$ and $\hat{S}_2(b)$ as an intermediate step. Thereafter, we estimate the standard model parameters $\hat{\theta}^{(2)}$ using Eq. (12). In contrast, in the second approach, $\hat{\theta}^{(1)}$, we fit the standard model directly to the direction DW signals as in Eq. (14) to estimate $\hat{\theta}^{(1)}$, respectively. Note that the superscript denotes the number of estimation steps of the approach.

The estimation of $\hat{S}_{lm}(b)$ and $\hat{\theta}^{(1)}$ can be performed using the least-squares estimators of Eqs. (13) and (14), respectively. However, to account for Rician signal biases,

we will compare such estimators to the CLS estimators, $\hat{\theta}_{RBC}^{(1)}$ and $\hat{\theta}_{RBC}^{(2)}$, which model the Rician expectation value operator at the relevant steps. Following Eq. (17), the Rician bias correction requires prior knowledge of the noise level. For simulated data, we know this value by design, whereas for the experimental data, we use the noise levels as estimated in Section 3.2.2.

All code was implemented using standard library functions from the optimization toolbox of *MATLAB* (Version: 23.2.0, R2023b; MathWorks, Natick, MA, USA).

3.4 | Statistical analyses

In this study, we measure the test/retest repeatability of estimators, and we quantify the agreement between two sets of measurements to quantify the robustness of the estimators to variations in scan protocols. The agreement between scan protocols is done by using half of the last b-shell ($b = 6 \, \text{ms}/\mu\text{m}^2$) gradient directions. We will use the coefficient of variation between two repeated measurements to measure test/retest reproducibility, whereas Lin's concordance correlation coefficient (CCC)⁷⁶ is used to measure agreement between two paired measurements.

3.4.1 | Test/retest repeatability

To assess the repeatability and reliability of the metrics, the coefficient of variation was computed as follows:

$$COV = \frac{\sqrt{\pi}}{N_s} \sum_{i=1}^{N_s} \frac{\left| x_i - x_i' \right|}{x_i + x_i'} \times 100 \, [\%]$$
 (18)

where x_i and x'_i are the test and retest measurements of a diffusion metric-of-interest of the *i*th subject, respectively, and N_s is the number of subjects.

3.4.2 | Concordance

The agreement between two subject-matched sets of measurements of a diffusion metric of interest was computed as follows:

$$\rho_C = \frac{2\rho\sigma_x\sigma_y}{(\mu_X - \mu_Y)^2 + \sigma_X^2 + \sigma_Y^2},\tag{19}$$

where ρ is the Pearson's correlation coefficient between X and Y; μ_X and μ_Y are the average values; and σ_X and σ_Y are the standard deviations. The values of X and Y are both $[N_s, 1] \in \Re^N$ vectors, representing a diffusion metric for each subject and measurement.

4 | RESULTS

4.1 | Simulations: Thermal noise effect on RISH features

Figure 1 shows the effect of signal noise on the accuracy and precision of $\hat{S}_0(b)$ and $\hat{S}_2(b)$ for a wide range of b-values and parameter values (n = 100.000, sampled from distributions defined in Section 3.1 in relation to distribution of the dMRI data and the used estimator (LLS versus CLS). We observe an SNR-dependent overestimation of $\hat{S}_0(b)$ if the dMRI data are Rician-distributed but an ordinary LLS estimator has been used to estimate $\hat{S}_{lm}(b)$. The error is significantly reduced when using the CLS estimator instead. In contrast, $\hat{S}_2(b)$ is prone to error, even in the case of Gaussian-distributed dMRI data. We observe SNR-dependent overestimation of $\hat{S}_2(b)$ with a magnitude of error that is inversely proportional to its underlying value $S_2(b)$. Rician signal biases result in an underestimation of $\hat{S}_2(b)$, with a magnitude that is proportional to $S_2(b)$. The use of a Rician bias-correcting estimator does not mitigate the bias introduced by taking the magnitude of noisy SH coefficients.

Figure 2 outlines the effect of SNR, number of gradient directions, and p_2 on $\hat{S}_0(b)$ and $\hat{S}_2(b)$ for Gaussian and Rician-distributed dMRI data. In these single-fiber simulations (w=1), the following parameters were fixed to f = 0.75, $D_a = 2.5 \ \mu \text{m}^2/\text{ms}$, $D_e^{\parallel} \in 2 \ \mu \text{m}^2/\text{ms}$, and $D_e^{\perp} =$ $0.5 \mu m^2/ms$. When not varying, the number of gradient directions was set to 32 and SNR to 30. Moreover, p_2 was set to 0.2 or 0.6 when varying the number of gradient directions or SNR, respectively. First, we observe that the error in the estimation of $\hat{S}_0(b)$ depends on the SNR, and p_2 in the case of Rician-distributed data only. The Rician signal bias results in an overestimation of $\hat{S}_0(b)$, particularly at low SNR and high p_2 with relative errors up to 20%. The error in the estimation of $\hat{S}_2(b)$ depends on SNR, number of gradient directions, and p_2 . However, unlike $\hat{S}_0(b)$, $\hat{S}_2(b)$ is subject to such errors even in the case of Gaussian-distributed dMRI data. Indeed, for Gaussian-distributed dMRI, we observe an overestimation $\hat{S}_2(b)$ that increases with decreasing SNR, number of gradient directions, and p_2 . In the case of Rician-distributed dMRI data, this overestimation is counterbalanced, oftentimes resulting in underestimation of $\hat{S}_2(b)$. This effect is most pronounced at low SNR and high p_2 .

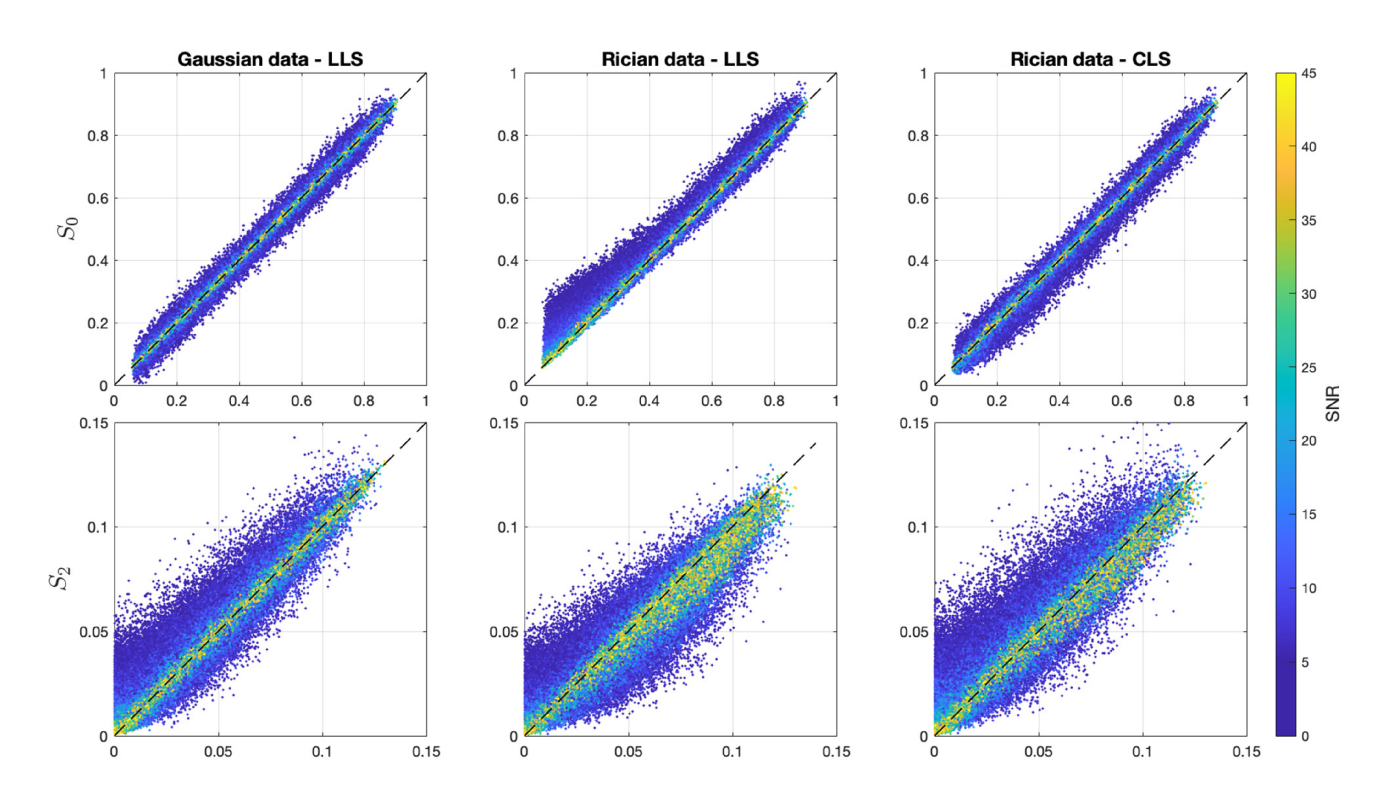


FIGURE 1 Rotational invariants S_0 and S_2 estimates against their ground truth for varying b-values and signal-to-noise ratio (SNR) levels: Gaussian noise with linear least squares (LLS) estimation (left), Rician noise with LLS estimation (middle), and Rician noise with conditional least squares (CLS) estimation (right). Top row: Behavior of S_0 . Under Gaussian noise, estimates are unbiased. Under Rician noise, however, low S_0 values are systematically overestimated. This bias is corrected when using CLS estimators, restoring an unbiased behavior. Bottom row: Behavior of S_2 . Even under Gaussian noise, S_2 tends to be overestimated at low values. Under Rician noise, two sources of bias emerge: Overestimation at low S_2 values and underestimation at high values. Applying CLS to Rician data mitigates the second source of bias, restoring the estimation pattern observed in the Gaussian case.

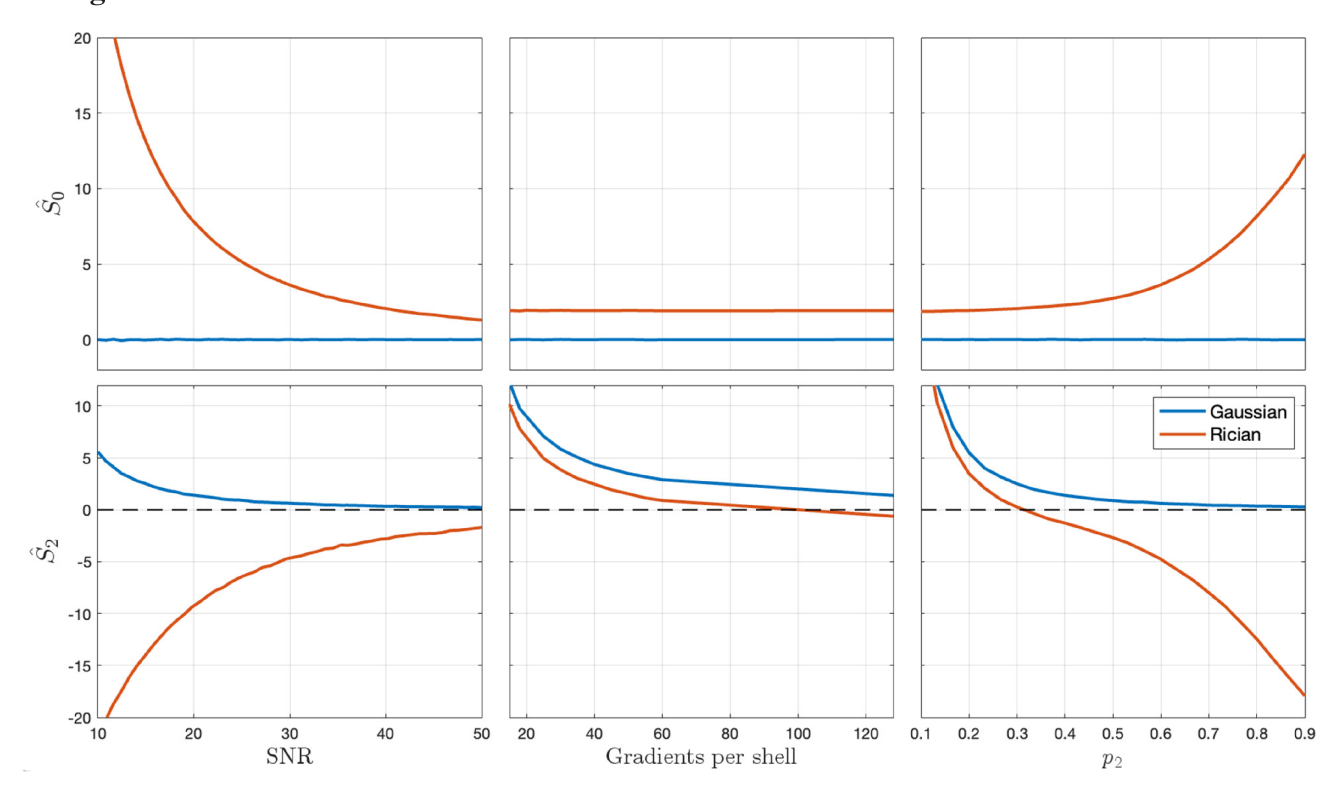


FIGURE 2 Relative error of S_0 and S_2 estimates for b = 6 ms/ μ m² varying signal-to-noise ratio (SNR; left), varying number of gradients per shell (middle), and varying p_2 (right). When not varying, the number of gradient directions was set to 32 and SNR to 30. Also, p_2 was set to 0.2 or 0.6 when varying the number of gradient directions or SNR, respectively. $Top\ row$: Behavior of S_0 . Gaussian noise is unbiased in all scenarios. Under Rician noise, however, S_0 is overestimated in all three cases. The overestimation diminishes for increasing SNR and decreasing axon dispersion p_2 . The number of gradients per shell does not affect the overestimation. $Bottom\ row$: Behavior of S_2 . Under Gaussian noise, S_2 is systematically overestimated, and such overestimation diminishes with increasing SNR, number of gradients per shell, and axon dispersion p_2 . Under Rician noise, however, more complex interactions come into play.

4.2 | Simulations: Thermal noise effect on biophysical modeling parameters across estimators

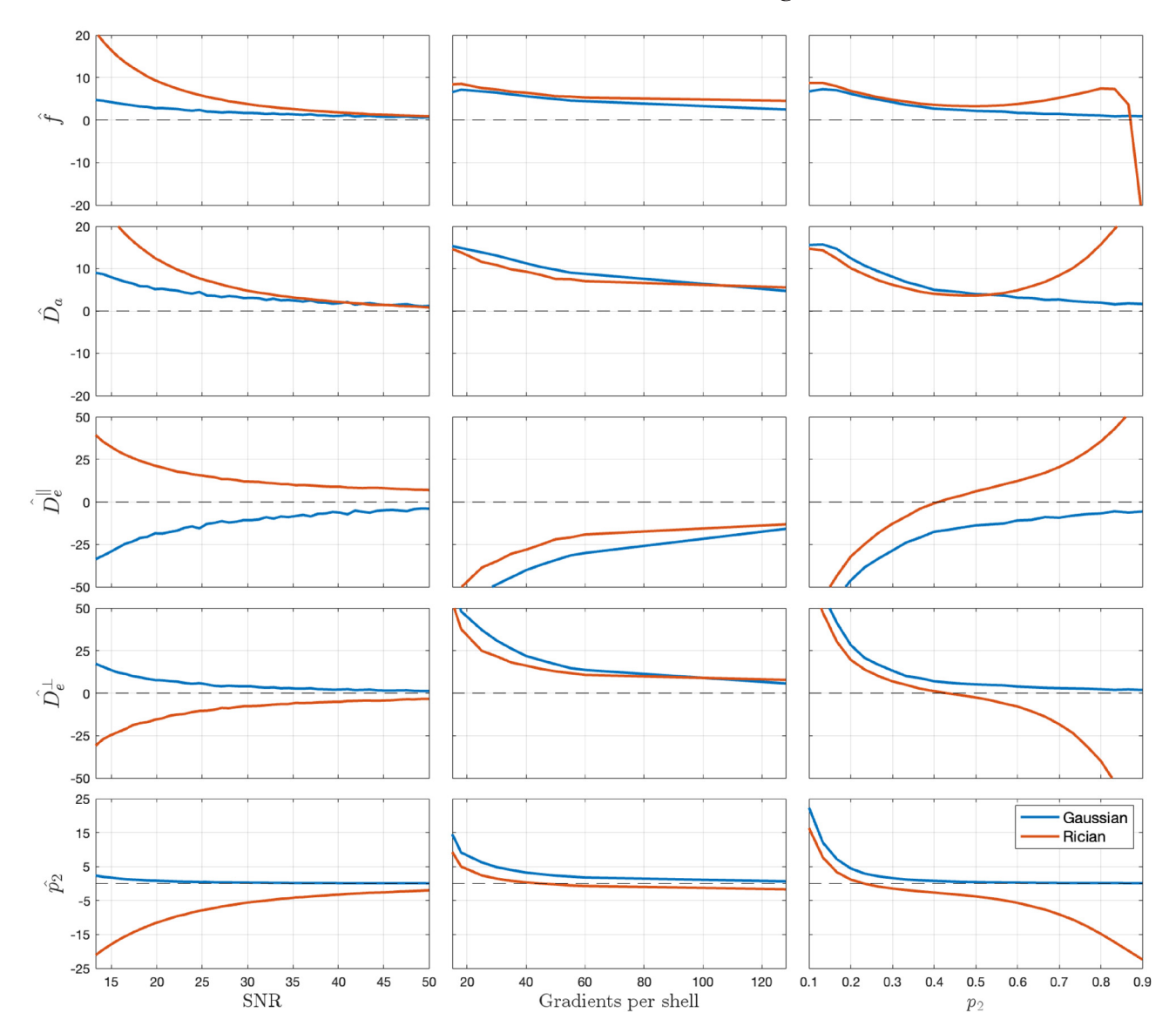
Figure 3 illustrates how the errors in the estimation of $\hat{S}_0(b)$ and $\hat{S}_2(b)$ propagate and affect the accuracy of $\hat{\boldsymbol{\theta}}^{(2)}$ (i.e., SH-based) estimators. Using the same simulated data as used for Figure 2, we demonstrate the effect of SNR, number of gradient directions, and p_2 on $\widehat{\boldsymbol{\theta}}^{(2)}$ for Gaussian and Rician-distributed dMRI data. As $\hat{\theta}^{(2)}$ is derived from $\hat{S}_0(b)$ and $\hat{S}_2(b)$ simultaneously, we observe errors in the case of Gaussian and Rician-distributed dMRI data, but the direction and magnitude of the error depends on the data distribution. However, even for Gaussian-distributed data, estimation errors increase across all parameters as SNR, number of gradients, or p_2 decrease, with errors ranging from a few percent to over 50%. For Rician-distributed dMRI data, the magnitude of the errors typically increases. However, instead of an overestimation, we observe an underestimation of \widehat{D}_e^{\perp} and \widehat{p}_2 . Although $\widehat{\boldsymbol{\theta}}^{(2)}$ had relatively low errors for high p_2 values under Gaussian-distributed data, we observe a strong error increase for Rician-distributed data.

Figure 4 presents violin plots of the error in the estimation of $\hat{\theta}^{(2)}$, $\hat{\theta}_{RBC}^{(2)}$, and $\hat{\theta}_{RBC}^{(1)}$ for a wide range of parameter values (n=1500, sampled from distributions defined in Section 3.1). All simulated dMRI data were Rician-distributed with randomly varying SNR. In addition, we computed the mean squared error (Table 1). For all metrics, the mean squared error—a measure that combines accuracy and precision—was lowest for $\hat{\theta}_{RBC}^{(1)}$, indicating superior overall performance.

4.3 | In vivo results

Figure 5 renders the in vivo maps of the different estimates for a single subject's white matter, overlapped with its grayscale FA. Overall, we observe a substantial noisy behavior on the original $\hat{\theta}^{(2)}$, probably intensified by the degeneracy of the problem and the inability of the branch





Percentage relative error in $\hat{\theta}^{(2)}$ microstructural estimates for Gaussian-distributed and Rician-distributed data for varying levels of signal-to-noise ratio (SNR; left), number of gradients per shell (middle), and axon dispersion p₂ (right). When not varying, the number of gradient directions was set to 32 and SNR to 30; p₂ was set to 0.2 or 0.6 when varying the number of gradient directions or SNR, respectively. Errors arise from inaccuracies in both $S_0(b)$ and $S_2(b)$, with Gaussian data showing increasing overestimation as SNR, number of directions, or p_2 decrease. Rician noise leads to generally larger errors, typically manifesting as underestimation, particularly at low SNR and high p_2 .

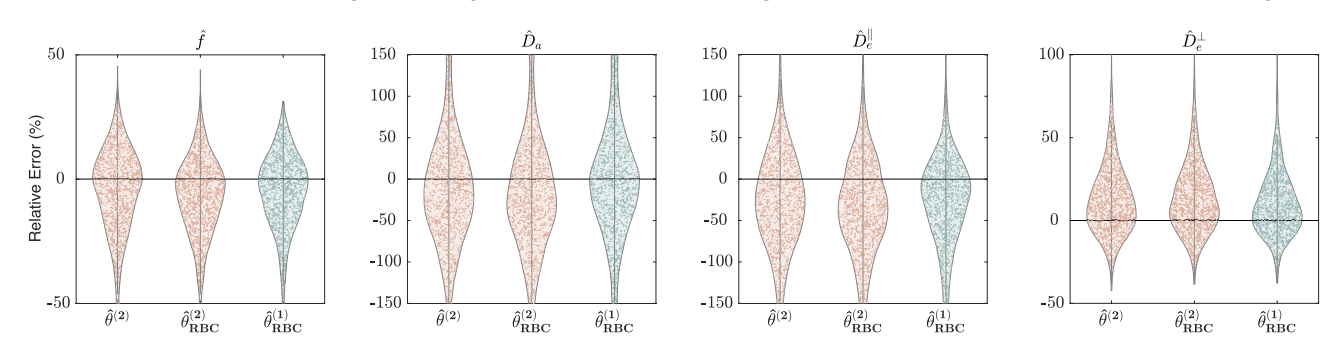


FIGURE 4 Relative error distributions of Standard Model Imaging microstructural estimates. Solid black line represents the ground truth (relative error equal to 0). Violin plots show errors in $\hat{\theta}^{(2)}$, $\hat{\theta}_{RBC}^{(2)}$, and $\hat{\theta}_{RBC}^{(1)}$ across 1500 Rician-distributed diffusion MRI simulations with varying parameters. The estimates' modes derived from $\hat{\theta}^{(2)}$ and $\hat{\theta}_{RBC}^{(2)}$ show consistent bias, in contrast to the unbiased estimates obtained from $\widehat{\boldsymbol{\theta}}_{RBC}^{(1)}$.

.5222594, 0, Downloaded from https://onlinelibrary.wiley.com/doi/10.1002/mrm.70035 by Universidad De Valladolid, Wiley Online Library on [06/10/2025]. See the Terms and Conditions (https://onlinelibrary.wiley.com/terms

and-conditions) on Wiley Online Library for rules of use; OA articles are governed by the applicable Creative Commons

selection algorithm to correctly decide the solution. In comparison, $\widehat{\theta}_{RBC}^{(2)}$ and $\widehat{\theta}_{RBC}^{(1)}$ depict more robust and stable maps throughout the white matter. Although the

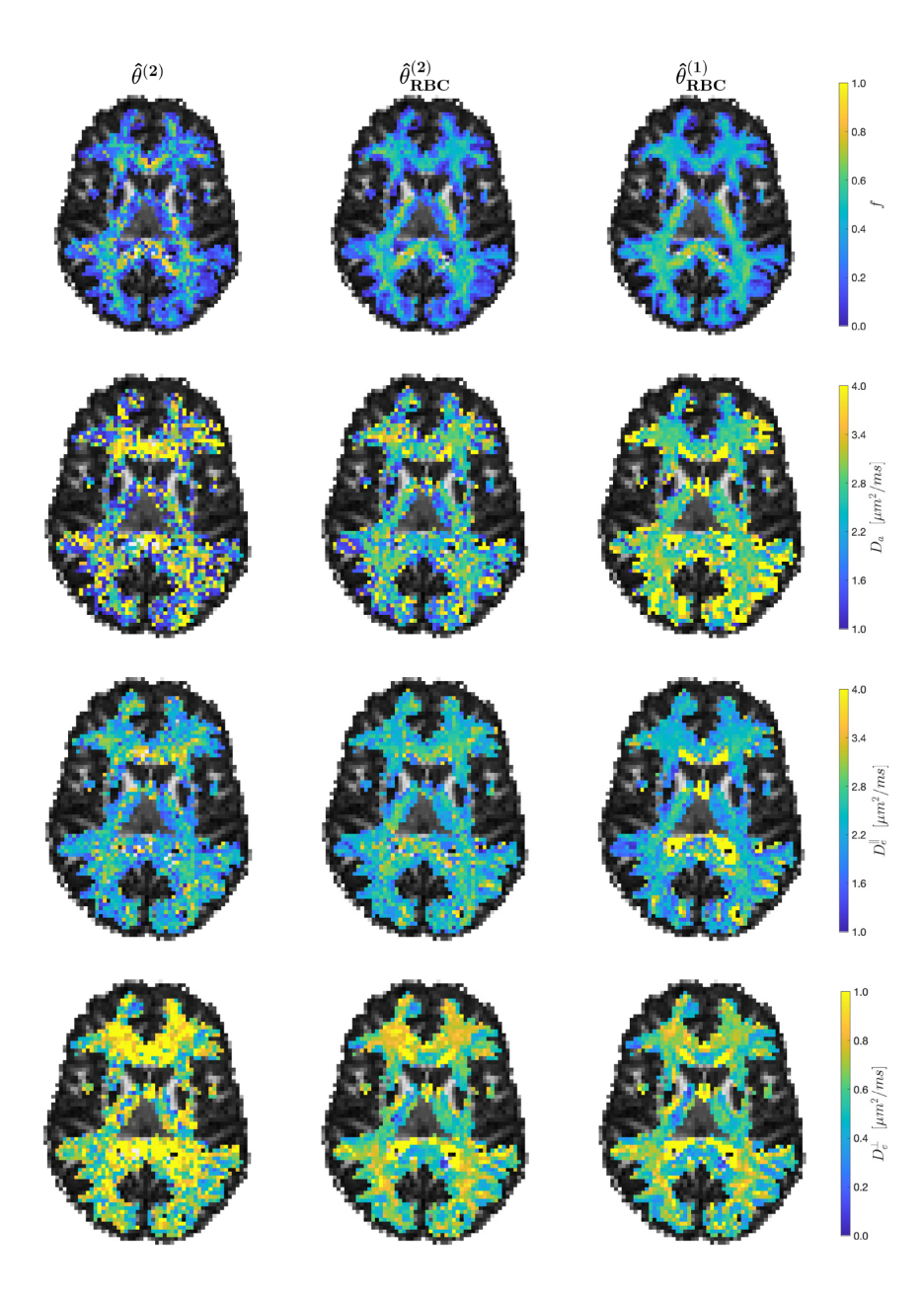
TABLE 1 Mean square error (MSE) of the estimated biophysical model parameters using simulated data with a wide range of underlying parameters. The value of $\widehat{m{ heta}}_{RBC}^{(1)}$ outperforms the other strategies by resulting in the lower MSE. Bold values depict the lowest MSE values for a given parameter.

| MSE | f | D_a | D_e^{\parallel} | D_e^\perp |
|--|--------|--------|-------------------|-------------|
| $\widehat{m{	heta}}^{(2)}$ | 0.0124 | 0.1704 | 0.2075 | 0.0262 |
| $\widehat{m{	heta}}_{	ext{RBC}}^{(2)}$ | 0.0152 | 0.2445 | 0.2858 | 0.0311 |
| $\widehat{m{	heta}}_{	ext{RBC}}^{(1)}$ | 0.0064 | 0.1085 | 0.1119 | 0.0115 |

difference on stability/robustness between $\widehat{m{ heta}}^{^{(2)}}$ and the other strategies can be observed in any of the maps, it is more prominent in the f and D_e^{\perp} parameters.

4.4 Protocol dependency

Table 2 reports Lin's CCC score obtained for each of the methods. From the three methods under study, $\hat{\theta}_{RBC}^{(1)}$ outperforms the other methods nominally for all SMI metrics. Following the guidelines for interpretation,⁷⁷ the performance of $\widehat{\boldsymbol{\theta}}_{RBC}^{(1)}$ ranges from substantial (0.95–0.99) to almost perfect. The performance of $\widehat{ heta}_{RBC}^{(2)}$ is more variable, ranging from poor to substantial, whereas $\widehat{\boldsymbol{\theta}}^{(2)}$ is overall poor.



Real data comparison of FIGURE 5 the estimation strategies. Comparison among the three approaches under study of microstructural estimates from in vivo data, masked via white-matter tract density imaging; see more in Section 3). Noticeably, $\hat{\boldsymbol{\theta}}^{(2)}$ outputs noisier maps, probably due to the degenerate landscape of the problem. This is mitigated in the proposed strategies $(\widehat{m{ heta}}_{RBC}^{(2)}$ and $\widehat{m{ heta}}_{RBC}^{(1)}$), which result in more robust maps.

4.5 | Reproducibility analysis

Figure 6 shows the COV between ROI medians within test–retest sessions for $\widehat{\theta}_{RBC}^{(2)}$ and $\widehat{\theta}_{RBC}^{(1)}$. To show the general trend, we perform a weighted linear fit, where the weights are defined by the number of voxels enclosed within each region. We observe an improved test/retest repeatability when using $\widehat{\theta}_{RBC}^{(1)}$, in particular for the intracellular model parameters. The fit line slope remains below 0.5 in all cases except D_e^{\parallel} (the slope is 1.12), implying an improved reproducibility of $\widehat{\theta}_{RBC}^{(1)}$ with respect to $\widehat{\theta}_{RBC}^{(2)}$. The average COV is 25.5% for the $\widehat{\theta}_{RBC}^{(2)}$, 5.8% for $\widehat{\theta}_{RBC}^{(2)}$, and 3.12% for $\widehat{\theta}_{RBC}^{(1)}$.

5 | DISCUSSION

To promote the use of rotational invariants in downstream analyses, support more specific inferences, and maximize their intersite and intrasite reproducibility, we must understand the confounds in their quantification, including their robustness to experimental factors such as SNR or

TABLE 2 Lin's concordance correlation coefficient (CCC) of the estimates from the full acquisition protocol against the halved last shell protocol. The value of $\hat{\theta}_{RBC}^{(1)}$ outperforms the other strategies scoring from substantial to almost perfect results in all parameters. Bold values depict the highest CCC scores for a given parameter.

| CCC | f | D_a | D_e^{\parallel} | D_e^\perp |
|-------------------------------------|------|-------|-------------------|-------------|
| $\widehat{	heta}^{(2)}$ | 0.86 | 0.84 | 0.85 | 0.71 |
| $\widehat{	heta}_{	ext{RBC}}^{(2)}$ | 0.96 | 0.84 | 0.95 | 0.97 |
| $\widehat{	heta}_{	ext{RBC}}^{(1)}$ | 0.99 | 0.93 | 0.99 | 0.97 |

protocol design, as well as develop parameter estimators that have a high accuracy, precision, and robustness.

The so-called Rician signal biases are known to affect the accuracy of commonly used least-squares estimators of diffusion metrics. Various works have previously reported that ignoring the Rician data distributions in parameter estimation results in underestimated mean diffusivities and FA, overestimated kurtosis values, and loss of angular resolution. Here we complement previous works by evaluating the effect of Rician signal biases on RISH features and SMI parameters.

There are various strategies to mitigate the effect of the Rician signal bias. Real-valued MRI provides a promising avenue if the raw or complex MRI data are accessible⁵⁶; however, most often, there is a need for estimators that model the data distributions explicitly. Although MLE is a popular example due its favorable properties in terms of accuracy and precision, it has been shown that it is not compatible with the series of image-preprocessing steps that alter the data distribution before fitting.⁶⁵ In contrast, RBC—a CLS estimator that offsets the model prediction by the Rician expectation value operator—has been shown to be a more accurate 78 and efficient alternative in mitigating biases in various diffusion metrics, 50,78 which also applies to the estimation of SHs. However, the Rician bias correction of SH is insufficient to maximize the accuracy of S_2 .

We observe that S_0 is overestimated when not accounting for the Rician distribution of the DW data. The magnitude of the error depends on the SNR, underlying diffusion properties, and other factors that affect the nominal DW signal, including b-value and echo time. The effect of noise on S_2 is less trivial as multiple sources of error contribute. Overall, the Rician signal bias primarily

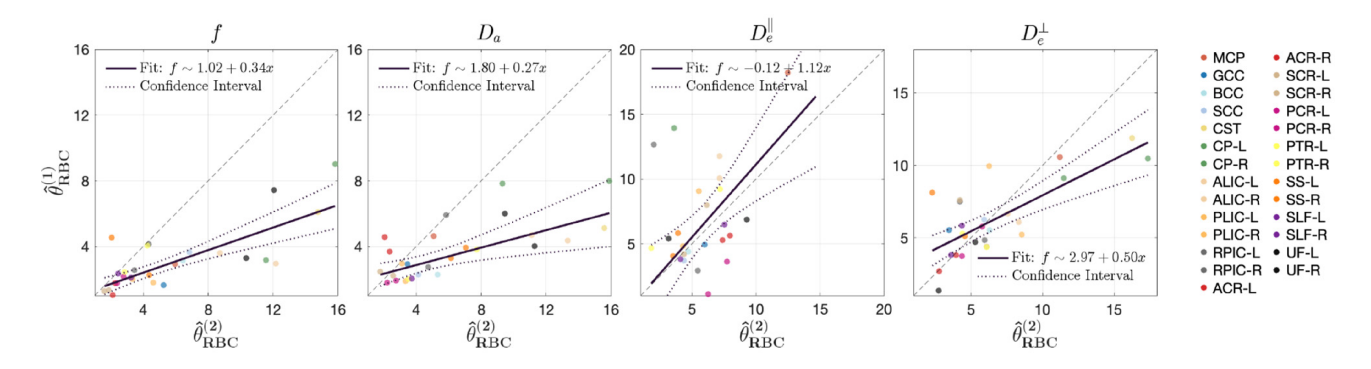


FIGURE 6 Test–retest reproducibility. Comparison of the coefficient of variation (COV) between the two red blood cell (RBC)–derived approaches for the four microstructural estimates from in vivo data. Colored dots depict COVs calculated from different regions of interest (ROIs; see legend). The full names of the ROIs are listed in Table S1 for completeness. Dashed black line represents x = y line. Black solid line represents the linear fit of the dots, weighted by the number of voxels enclosed within each region. Dotted black lines depict the 95% confidence intervals of the fit. As shown, $\hat{\theta}_{RBC}^{(1)}$ consistently results in similar or smaller COV values, resulting in fitting lines that range from the identity line to slopes smaller than one. Thus, test–retest repeatability does not decrease with the proposed $\hat{\theta}_{RBC}^{(1)}$ strategy.

results in an underestimation of S_2 , primarily in voxels with high anisotropy, when compared to simulations with Gaussian-distributed data. Given the high correlation between S_2 and FA, it is not surprising that similar trends have been observed in previous DTI studies. However, when S_2 is low, such as in crossing fibers or isotropic structures, there is a significant overestimation of S_2 , which is further amplified at low SNR or low number of gradient directions. Indeed, S_2 is vulnerable to a secondary source of noise bias that affects its accuracy. All SH coefficient estimates are intrinsically noisy, and their noise level depends on the gradient-encoding schemes. The noise on each individual SH coefficient is asymptotically Gaussian, but the computation of the rotational invariant features skews the noise distribution if the order is larger than 0. Hence, the expectation value of S_2 exceeds its underlying value.^{37,59} The offset depends on the underlying value and noise level of the SH coefficients, which in turn depends on the SNR of the dMRI data and the number of gradient directions. The dependency of the errors in the estimation of S_0 and S_2 on SNR, scan protocol settings, and/or microstructure is a barrier to data harmonization and reproducibility of diffusion metrics in a wide range of applications.

The RISH features are commonly used as a basis for biophysical modeling. Therefore, any of these biases might affect the accuracy, the reproducibility, and intersite comparison of metrics derived from the models. Here, we focus our evaluation of such effects on SMI parameters. Given that SMI builds on S_0 and S_2 , it is vulnerable to both sources of biases. Indeed, when simulating Gaussian-distributed noise, p_2 and D_a are underestimated, whereas f and D_e^{\parallel} are overestimated. Similar biases are observed when using a Rician bias-correcting estimator in the case of Rician-distributed data. The magnitude of the effects is dependent on the SNR, protocol, and underlying microstructure. The Rician bias itself might amplify or mask any of such effects, as it independently biases the parameters as follows: increased f, D_a and D_e^{\parallel} , and decreased D_e^{\perp} and p_2 . To maximize the accuracy and robustness of SMI parameters across protocols and studies, it is critical to minimize both noise biases.

Leysen et al. presented a voxel-wise Rank-1 decomposition of SH coefficients of the DW signal to lower their noise level, hence improving the accuracy of higher-order RISH features. Denoising the raw data or optimizing the experimental design favoring a large number of DW gradients per *b*-shell will also improve the accuracy of biophysical models that are derived from RISH features. Although favorable, none of these approaches will resolve the effect in their entirety and might not be feasible in limited scan times. Here, we evaluate an alternative fitting strategy for SMI that avoids the use of SH projections as an intermediate step, thereby evading the secondary source of

noise. Despite its increased dimensionality, this alternative strategy shows an improved robustness to noise, reduced prevalence of degenerate solutions, enhanced consistency across estimates from different protocol acquisitions, and an improved test/retest repeatability scores when compared with SH-based SMI (see Figures 4 to 6 and Tables 1 and 2). However, the accuracy of the estimator will depend on the adequacy of the selected SH order to capture the complexity of the underlying WM configuration. Therefore, we recommend its use in DW data with sufficiently dense sampling of gradient directions. ⁸⁰

The intermediate use of RISH features was initially motivated by the decreased dimensionality of the model. Indeed, by disentangling the microstructural kernel from the fiber ODF, the number of parameters that are to be estimated drops significantly. However, here we show that the simultaneous estimation of both the microstructural kernel and the fiber ODF does not negatively affect the precision of the typical microstructural parameters: f, D_a , D_e^{\parallel} , and D_e^{\perp} . Instead, following our experimental data, we observe that maps are overall cleaner and less contaminated by the significant degeneracies that are commonly observed in SMI. Moreover, the proposed method offers the opportunity for an integration of microstructure and tractography by means of an fODF estimation, without the need of a globally estimated kernel. It must be noted, however, that the proposed model might be less tuned to the use of alternative estimators, including machine learning approaches. 18,27,81-83

A key limitation of this study is that the use of this estimator requires prior information on the data that are not always available. Before parameter estimation, (i) it must be verified that the data of the unprocessed magnitude MRI are Rician distributed, and (ii) the noise level is assumed to be known. In our study, we adopted the MPPCA technique for noise map estimation, as it has been shown to be accurate if applied to uncorrelated Gaussian distributed data. The error in the noise level has shown to be as low as 1%.67 In that case, the downstream effect on SMI parameters using RBC is below 0.5%. To meet that requirement, we estimated the noise level from the lower b-values only. Note, however, that other estimators might also be used if proven accurate and can be used interchangeably (e.g., Pieciak et al.⁸⁴ under the assumption of Rician-distributed data or Henriques et al.85 in the case of correlated noise).

Moreover, we evaluated the downstream effect of biases in RISH features on SMI parameters using realistic scan protocols. However, it is important to note that $\hat{\theta}^{(1)}$ only exhibits asymptotic normality and consistency.⁶⁵ As our accuracy measures are based on normality assumptions (e.g., mean of distribution), minimal scan protocols

may give the appearance of inaccurate estimates. These errors, however, tend to diminish as the number of gradient directions and/or b-values increases, with estimates converging to the right solution. We further hypothesize that our findings can be translated to other models that currently use a two-step fitting process centered around RISH features, including axon diameter mapping, 32 SANDI, 18 NEXI, 19 SMEX, 35 and others.

In summary, we evaluated the effect of thermal noise on widely used RISH features and its effect on derived biophysical models such as the SMI. We propose an alternative fitting strategy bypassing RISH features and correcting for Rician bias via CLS estimators that has proven to be not only more accurate and robust, but also equal or more repeatable across sessions and more reproducible across protocol acquisitions.

ACKNOWLEDGMENTS

This work was supported in part by the National Institute of Neurological Disorders and Stroke of the National Institutes of Health (NIH) under awards R01 NS088040 and was performed under the rubric of the Center for Advanced Imaging Innovation and Research (CAI2R, www.cai2r.net), an NIBIB National Center for Biomedical Imaging and Bioengineering (NIH P41 EB017183). The Connectom data were in part acquired at the UK National Facility for in vivo MR Imaging of Human Tissue Microstructure funded by the EPSRC (grant EP/M029778/1) and the Wolfson Foundation. Guillem París was funded by the Consejería de Educación de Castilla y León and the European Social Fund through the "Ayudas para financiar la contratación predoctoral de personal investigador - Orden EDU/1100/2017 12/12" program as well as by the mobility program "Movilidad de estudiantes de Doctorado UVa 2023." Tomasz Pieciak acknowledges the Polish National Agency for Academic Exchange for grant PPN/BEK/2019/1/00421 under the Bekker program and the Ministry of Science and Higher Education (Poland) under the scholarship for outstanding young scientists (692/STYP/13/2018).

FUNDING INFORMATION

This work was funded by Junta de Castilla and León and Fondo Social Europeo Plus (FSE+) under research grant VA156P24, and by grants PID2021-124407NB-I00 and TED2021-130758B-I00, funded by Ministerio de Ciencia e Innovación (Spain)/Agencia Estatal de Investigación (with DOI 10.13039/501100011033)/10.13039/501100011033 and the European Union "NextGenerationEU/Plan de Recuperación, Transformación y Resiliencia."

ORCID

Guillem París https://orcid.org/0000-0002-1564-1199
Tomasz Pieciak https://orcid.org/0000-0002-7543-3658
Derek K. Jones https://orcid.org/0000-0003-4409-8049
Santiago Aja-Fernández https://orcid.org/0000-0002
-5337-5071

Antonio Tristán-Vega https://orcid.org/0000-0002-4614

REFERENCES

- Le Bihan D. Looking into the functional architecture of the brain with diffusion MRI. *Int Congr Ser.* 2006;1290:1-24. doi:10.1016/j.ics.2006.04.006
- Nir TM, Jahanshad N, Villalon-Reina JE, et al. Effectiveness of regional DTI measures in distinguishing Alzheimer's disease, MCI, and normal aging. *NeuroImage Clin*. 2013;3:180-195. doi:10.1016/j.nicl.2013.07.006
- 3. Labate A, Cherubini A, Tripepi G, et al. White matter abnormalities differentiate severe from benign temporal lobe epilepsy. *Epilepsia*. 2015;56:1109-1116. doi:10.1111/epi.13027
- 4. Trojsi F, Caiazzo G, Corbo D, et al. Microstructural changes across different clinical milestones of disease in amyotrophic lateral sclerosis. *PLoS One*. 2015;10:e0119045. doi:10.1371/journal.pone.0119045
- Afzali M, Pieciak T, Newman S, et al. The sensitivity of diffusion MRI to microstructural properties and experimental factors. J Neurosci Methods. 2021;347:108951. doi:10.1016/j.jneumeth .2020.108951
- Lebel C, Treit S, Beaulieu C. A review of diffusion MRI of typical white matter development from early childhood to young adulthood. NMR Biomed. 2019;32:E3778.
- 7. Raven EP, Veraart J, Kievit RA, et al. In vivo evidence of microstructural hypo-connectivity of brain white matter in 22q11.2 deletion syndrome. *Mol Psychiatry*. 2023b;28:4342-4352. doi:10.1038/s41380-023-02178-w
- 8. Cox SR, Ritchie SJ, Tucker-Drob EM, et al. Ageing and brain white matter structure in 3,513 UK biobank participants. *Nat Commun.* 2016;7:1-13.
- Pieciak T, París G, Beck D, et al. Spherical means-based free-water volume fraction from diffusion MRI increases non-linearly with age in the white matter of the healthy human brain. *Neuroimage*. 2023;279:120324. doi:10.1016/j.neuroimage .2023.120324
- Le Bihan D, Iima M. Diffusion magnetic resonance imaging: what water tells us about biological tissues. *PLoS Biol*. 2015;13:E1002203.
- Jelescu IO, Budde MD. Design and validation of diffusion MRI models of white matter. Front Phys. 2017;5:61.
- Novikov DS, Kiselev VG, Jespersen SN. On modeling. Mag Reson Med. 2018b;79:3172-3193.
- Stanisz GJ, Wright GA, Henkelman RM, Szafer A. An analytical model of restricted diffusion in bovine optic nerve. *Mag Reson Med.* 1997;37:103-111.
- 14. Assaf Y, Basser PJ. Composite hindered and restricted model of diffusion (CHARMED) MR imaging of the human brain. *NeuroImage*. 2005;27:48-58.

- Jespersen SN, Kroenke CD, Østergaard L, Ackerman JJH, Yablonskiy DA. Modeling dendrite density from magnetic resonance diffusion measurements. *Neuroimage*. 2007;34:1473-1486. doi:10.1016/j.neuroimage.2006.10.037
- 16. Zhang H, Schneider T, Wheeler-Kingshott CA, Alexander DC. NODDI: practical in vivo neurite orientation dispersion and density imaging of the human brain. *NeuroImage*. 2012;61:1000-1016.
- Kaden E, Kelm ND, Carson RP, Does MD, Alexander DC. Multi-compartment microscopic diffusion imaging. *Neuroimage*. 2016b;139:346-359.
- 18. Palombo M, Ianus A, Guerreri M, et al. SANDI: a compartment-based model for non-invasive apparent soma and neurite imaging by diffusion MRI. *Neuroimage*. 2020;215:116835.
- Jelescu IO, de Skowronski A, Geffroy F, Palombo M, Novikov DS. Neurite exchange imaging (NEXI): a minimal model of diffusion in gray matter with inter-compartment water exchange. Neuroimage. 2022;256:119277.
- 20. Veraart J, Novikov DS, Fieremans E. TE dependent diffusion imaging (TEdDI) distinguishes between compartmental T_2 relaxation times. *Neuroimage*. 2018a;182:360-369. doi:10.1016/j .neuroimage.2017.09.030
- 21. Lampinen B, Szczepankiewicz F, Novén M, et al. Searching for the neurite density with diffusion MRI: challenges for biophysical modeling. *Hum Brain Mapp.* 2019;40:2529-2545.
- Jelescu IO, Veraart J, Fieremans E, Novikov DS. Degeneracy in model parameter estimation for multi-compartmental diffusion in neuronal tissue. NMR Biomed. 2016;29:33-47.
- Novikov DS, Veraart J, Jelescu IO, Fieremans E. Rotationally-invariant mapping of scalar and orientational metrics of neuronal microstructure with diffusion MRI. *Neu-roimage*. 2018a;174:518-538. doi:10.1016/j.neuroimage.2018.03
- 24. Fieremans E, Benitez A, Jensen JH, et al. Novel white matter tract integrity metrics sensitive to Alzheimer disease progression. *AJNR*. 2013;34:2105-2112.
- 25. Tariq M, Schneider T, Alexander DC, Gandini Wheeler-Kingshott CA, Zhang H. Bingham-NODDI: mapping anisotropic orientation dispersion of neurites using diffusion MRI. *Neuroimage*. 2016;133:207-223.
- 26. Mirzaalian H, de Pierrefeu A, Savadjiev P, et al. Harmonizing diffusion MRI data across multiple sites and scanners. *Lecture Notes in Computer Science*. Springer International Publishing; 2015:12-19. doi:10.1007/978-3-319-24553-9_2
- Reisert M, Kellner E, Dhital B, Hennig J, Kiselev VG. Disentangling micro from mesostructure by diffusion MRI: a
 Bayesian approach. *Neuroimage*. 2017;147:964-975. doi:10.1016
 /j.neuroimage.2016.09.058
- Reisert M, Kiselev VG, Dhital B. A unique analytical solution of the white matter standard model using linear and planar encodings. Magn Reson Med. 2019;81:3819-3825.
- Pizzolato M, Andersson M, Canales-Rodríguez EJ, Thiran JP, Dyrby TB. Axonal T2 estimation using the spherical variance of the strongly diffusion-weighted MRI signal. *Magn Reson Imaging*. 2022;86:118-134.
- 30. Veraart J, Raven E, Jones D, Palombo M. Axon diameter mapping is confounded by glial cells. In: *Proceedings of the Annual Meeting of ISMRM*; 2023. Abstract 0973. doi:10.58530/2023/0973

- Kaden E, Kruggel F, Alexander DC. Quantitative mapping of the per-axon diffusion coefficients in brain white matter. *Magn Reson Med*. 2016a;75:1752-1763.
- 32. Veraart J, Raven EP, Edwards LJ, Weiskopf N, Jones DK. The variability of MR axon radii estimates in the human white matter. *Hum Brain Mapp*. 2021;42:2201-2213.
- Pasternak O, Sochen N, Gur Y, Intrator N, Assaf Y. Free water elimination and mapping from diffusion MRI. Magn Reson Med. 2009;62:717-730. doi:10.1002/mrm.22055
- 34. Tristán-Vega A, París G, de Luis-García R, Aja-Fernández S. Accurate free-water estimation in white matter from fast diffusion MRI acquisitions using the spherical means technique. *Magn Reson Med.* 2021;87:1028-1035. doi:10.1002/mrm.28997
- 35. Olesen JL, Østergaard L, Shemesh N, Jespersen SN. Diffusion time dependence, power-law scaling, and exchange in gray matter. *Neuroimage*. 2022;251:118976. doi:10.1016/j.neuroimage.2022.118976
- Zucchelli M, Deslauriers-Gauthier S, Deriche R. A computational framework for generating rotation invariant features and its application in diffusion MRI. *Med Image Anal*. 2020;60:101597.
- 37. Pieciak T, París G, Tristán-Vega A, Aja-Fernández S. Unbiasing the spherical variance of a diffusion-weighted MR signal: an application to intra-axonal T₂ estimation. In: *Proceedings of the Annual Meeting of ISMRM & ISMRT, Singapore*; 2024.
- Coelho S et al. Assessment of precision and accuracy of brain white matter microstructure using combined diffusion MRI and relaxometry. ArXiv 2024 https://www.ncbi.nlm.nih.gov/pubmed/38463511
- Chamberland M, Genc S, Tax CMW, et al. Detecting microstructural deviations in individuals with deep diffusion MRI tractometry. *Nature Computational Sci.* 2021;1:598-606. doi:10.1038/s43588-021-00126-8
- 40. Ward IL, Raven EP, de la Rosa S, Jones DK, Teufel C, von dem Hagen E. White matter microstructure in face and body networks predicts facial expression and body posture perception across development. *Hum Brain Mapp*. 2023;44:2307-2322. doi:10.1002/hbm.26211
- 41. Mirzaalian H, Ning L, Savadjiev P, et al. Inter-site and inter-scanner diffusion MRI data harmonization. *Neuroimage*. 2016;135:311-323. doi:10.1016/j.neuroimage.2016.04.041
- 42. Karayumak SC, Bouix S, Ning L, et al. Retrospective harmonization of multi-site diffusion MRI data acquired with different acquisition parameters. *Neuroimage*. 2019;184:180-200. doi:10.1016/j.neuroimage.2018.08.073
- Balchandani P, Naidich TP. Ultra-high-field MR neuroimaging. AJNR. 2015;36:1204-1215.
- 44. Setsompop K, Kimmlingen R, Eberlein E, et al. Pushing the limits of in vivo diffusion MRI for the human connectome project. *Neuroimage*. 2013;80:220-233. doi:10.1016/j.neuroimage.2013.05.078
- Wiggins GC, Polimeni JR, Potthast A, Schmitt M, Alagappan V, Wald LL. 96-channel receive-only head coil for 3 tesla: design optimization and evaluation. *Magn Reson Med.* 2009;62: 754-762.
- Veraart J, Novikov DS, Christiaens D, Ades-aron B, Sijbers J, Fieremans E. Denoising of diffusion MRI using random matrix theory. *Neuroimage*. 2016a;142:394-406. doi:10.1016/j .neuroimage.2016.08.016

- Pierpaoli C, Basser PJ. Toward a quantitative assessment of diffusion anisotropy. Magn Reson Med. 1996;36:893-906. doi:10.1002/mrm.1910360612
- 48. Jones DK, Basser PJ. "Squashing peanuts and smashing pumpkins": how noise distorts diffusion-weighted MR data. *Magn Reson Med*. 2004;52:979-993.
- Veraart J, Van Hecke W, Sijbers J. Constrained maximum likelihood estimation of the diffusion kurtosis tensor using a Rician noise model. *Magn Reson Med.* 2011;66:678-686. doi:10.1002/mrm.22835
- Uhl Q, Pavan T, Molendowska M, Jones D, Palombo M, Jelescu I.
 Quantifying human gray matter microstructure using NEXI and 300 mT/m gradients. In: *Proceedings of the Annual Meeting of ISMRM*; 2024. Abstract 0685. doi:10.58530/2023/0685
- Tournier JD, Calamante F, Gadian DG, Connelly A. Direct estimation of the fiber orientation density function from diffusion-weighted MRI data using spherical deconvolution. *Neuroimage*. 2004;23:1176-1185. doi:10.1016/j.neuroimage.2004 .07.037
- 52. Veraart J, Fieremans E, Rudrapatna U, Jones DK, Novikov DS. Unbreaking the power law scaling of the dMRI signal on the connectom scanner reveals its sensitivity to axon diameters. In: Proceedings of the Annual Meeting of ISMRM & ISMRT, Paris; 2018. Abstract 0252.
- 53. Hobson EW. *The Theory of Spherical and Ellipsoidal Harmonics*. Cambridge University Press; 2012.
- 54. Tournier JD, Smith R, Raffelt D, et al. MRtrix3: a fast, flexible and open software framework for medical image processing and visualisation. *NeuroImage*. 2019;202:116137.
- Henriques RN, Tax CMW, Shemesh N, Veraart J. Biophysical modeling of the white matter: from theory towards clinical practice. 2018 In: *Proceedings of the 27th ISMRM Annual Meeting*, Montreal, Canada, Abstract #1008.
- Eichner C, Cauley SF, Cohen-Adad J, et al. Real diffusion-weighted MRI enabling true signal averaging and increased diffusion contrast. *Neuroimage*. 2015;122:373-384. doi:10.1016/j.neuroimage.2015.07.074
- Aja-Fernández S, Vegas-Sánchez-Ferrero G. Filtering and Estimation. Statistical Analysis of Noise in MRI: Modeling. Springer; 2016.
- 58. Gudbjartsson H, Patz S. The Rician distribution of noisy MRI data. *Magn Reson Med.* 1995;34:910-914.
- Tristán-Vega A, Aja-Fernández S, Westin C-F. Least squares for diffusion tensor estimation revisited: propagation of uncertainty with Rician and non-Rician signals. *Neuroimage*. 2012;59:4032-4043. doi:10.1016/j.neuroimage.2011.09.074
- 60. Kerkelä L, Henriques RN, Hall MG, Clark CA, Shemesh N. Validation and noise robustness assessment of microscopic anisotropy estimation with clinically feasible double diffusion encoding MRI. Magn Reson Med. 2020;83:1698-1710.
- Cordero-Grande L, Christiaens D, Hutter J, Price AN, Hajnal JV.
 Complex diffusion-weighted image estimation via matrix recovery under general noise models. *NeuroImage*. 2019;200:391-404.
- 62. Moeller S, Pisharady PK, Ramanna S, et al. NOise reduction with Distribution corrected (NORDIC) PCA in dMRI with complex-valued parameter-free locally low-rank processing. *NeuroImage*. 2021;226:117539.
- Varadarajan D, Haldar JP. A majorize-minimize framework for Rician and non-central chi MR images. *IEEE Trans Med Imag*ing. 2015;34:2191-2202.

- Sijbers J, den Dekker AJ, Scheunders P, Van Dyck D. Maximum-likelihood estimation of Rician distribution parameters. *IEEE Trans Med Imaging*. 1998;17:357-361. doi:10.1109/42.712125
- Veraart J, Rajan J, Peeters RR, Leemans A, Sunaert S, Sijbers J. Comprehensive framework for accurate diffusion MRI parameter estimation. *Magn Reson Med*. 2013;70:972-984.
- Koay CG, Basser PJ. Analytically exact correction scheme for signal extraction from noisy magnitude MR signals. *J Magn Reson*. 2006;179:317-322.
- Veraart J, Fieremans E, Novikov DS. Diffusion MRI noise mapping using random matrix theory. *Magn Reson Med*. 2016b;76:1582-1593.
- Henriques RN, Jespersen SN, Jones DK, Veraart J. Toward more robust and reproducible diffusion kurtosis imaging. Magn Reson Med. 2021;86:1600-1613. doi:10.1002/mrm.28730
- 69. Walsh DO, Gmitro AF, Marcellin MW. Adaptive reconstruction of phased array MR imagery. *Magn Reson Med.* 2000;43:682-690. doi:10.1002/(sici)1522-2594(200005)43:5
- Andersson JLR, Graham MS, Zsoldos E, Sotiropoulos SN. Incorporating outlier detection and replacement into a non-parametric framework for movement and distortion correction of diffusion MR images. *Neuroimage*. 2016;141:556-572.
- Kellner E, Dhital B, Kiselev VG, Reisert M. Gibbs-ringing artifact removal based on local subvoxel-shifts. Magn Reson Med. 2015;76:1574-1581. doi:10.1002/mrm.26054
- Andersson JLR, Skare S, Ashburner J. How to correct susceptibility distortions in spin-echo echo-planar images: application to diffusion tensor imaging. *Neuroimage*. 2003;20: 870-888.
- Rudrapatna U, Parker GD, Roberts J, Jones DK. A comparative study of gradient nonlinearity correction strategies for processing diffusion data obtained with ultra-strong gradient MRI scanners. *Magn Reson Med.* 2020;85:1104-1113. doi:10.1002/mrm.28464
- 74. Oishi K, Zilles K, Amunts K, et al. Human brain white matter atlas: identification and assignment of common anatomical structures in superficial white matter. *Neuroimage*. 2008;43:447-457. doi:10.1016/j.neuroimage.2008.07.009
- 75. Calamante F, Tournier J-D, Jackson GD, Connelly A. Track-density imaging (TDI): super-resolution white matter imaging using whole-brain track-density mapping. *Neuroimage*. 2010;53:1233-1243. doi:10.1016/j.neuroimage.2010.07.024
- Lawrence I, Lin K. A concordance correlation coefficient to evaluate reproducibility. *Biometrics*. 1989;45:255-268.
- Akoglu H. User's guide to correlation coefficients. Turk J Emerg Med. 2018;18:91-93. doi:10.1016/j.tjem.2018.08.001
- 78. Veraart J, Van Cauter S, Sunaert S, Sijbers J. Conditional least squares estimation of diffusion MRI parameters. In: *Proceedings of the 20th Annual Meeting of ISMRM, Melbourne, Australia*; 2012. Abstract #3575.
- 79. Leysen S, Sunaert S, Maes F, Christiaens D. Voxel-level denoising of diffusion MRI using a rank-1 decomposition. In: *Proceedings of the Annual Meeting of ISMRM*; 2023. Abstract 5016.
- 80. Tournier JD, Calamante F, Connelly A. Determination of the appropriate b value and number of gradient directions for high-angular-resolution diffusion-weighted imaging. *NMR Biomed*. 2013;26:1775-1786. doi:10.1002/nbm.3017
- 81. Nedjati-Gilani GL, Schneider T, Hall MG, et al. Machine learning based compartment models with permeability for white

- matter microstructure imaging. *Neuroimage*. 2017;150:119-135. doi:10.1016/j.neuroimage.2017.02.013
- 82. de Almeida Martins JP, Nilsson M, Lampinen B, et al. Neural networks for parameter estimation in microstructural MRI: application to a diffusion-relaxation model of white matter. *Neuroimage*. 2021;244:118601. doi:10.1016/j.neuroimage.2021.118601
- 83. Coelho S, Baete SH, Lemberskiy G, et al. Reproducibility of the standard model of diffusion in white matter on clinical MRI systems. *Neuroimage*. 2022;257:119290. doi:10.1016/j.neuroimage.2022.119290
- 84. Pieciak T, Aja-Fernandez S, Vegas-Sanchez-Ferrero G. Non-stationary rician noise estimation in parallel MRI using a single image: a variance-stabilizing approach. *IEEE Trans Pattern Anal Mach Intell*. 2017;39:2015-2029. doi:10.1109/tpami.2016.2625789
- 85. Henriques RN, Ianuş A, Novello L, Jovicich J, Jespersen SN, Shemesh N. Efficient PCA denoising of spatially correlated redundant MRI data. *Imaging Neurosci.* 2023;1:1-26. doi:10.1162/imag_a_00049

SUPPORTING INFORMATION

Additional supporting information may be found in the online version of the article at the publisher's website.

Table S1. List of the 27 regions of interest (ROIs) analyzed in this work (see Figure 6), showing their corresponding abbreviations and full anatomical names.

How to cite this article: París G, Pieciak T, Jones DK, Aja-Fernández S, Tristán-Vega A, Veraart J. Thermal noise lowers the accuracy of rotationally invariant harmonics of diffusion MRI data and their robustness to experimental variations. *Magn Reson Med*. 2025;1-16. doi: 10.1002/mrm.70035